



Cite this: *J. Mater. Chem. A*, 2016, 4, 7903

Achieving high efficiency and improved stability in large-area ITO-free perovskite solar cells with thiol-functionalized self-assembled monolayers†

Chih-Yu Chang,^{*a} Yu-Chia Chang,^a Wen-Kuan Huang,^a Wen-Chi Liao,^a Hung Wang,^a Chieh Yeh,^a Bo-Chou Tsai,^a Yu-Ching Huang^b and Cheng-Si Tsao^{bc}

We report a novel protocol for achieving highly efficient and stable indium-tin-oxide (ITO)-free large-area perovskite solar cells (PeSCs) by introducing thiol-functionalized self-assembled monolayers (SAMs) to modify the interfacial properties of the devices. Two SAM molecules, 3-mercaptopropyltrimethoxysilane (MPTMS) and (11-mercaptoundecyl)trimethylammonium bromide (MUTAB), are employed as the seed layer for an ultrathin Ag transparent electrode and cathode buffer layer (CBL), respectively. Our results indicate that both SAMs can afford admirable interfacial properties. The thiol groups on the MPTMS SAM can interact with the incident Ag atoms, thereby lowering the percolation thickness of the Ag film to 8 nm. The resulting ultrathin Ag film provides several remarkable features for use as the transparent electrode in PeSCs, including a low resistance of $\sim 6 \Omega \text{ sq}^{-1}$, high average transmittance up to $\sim 78\%$, and high robustness against solvents and mechanical deformation. In addition to using the MPTMS SAM as the seed layer, the double-end functionalized MUTAB can not only covalently bond to the Ag surface for SAM formation, but also induce the formation of favorable interfacial dipoles to turn a high work-function (WF) Ag electrode into an efficient low-WF electrode. With these desired interfacial properties, the resulting devices deliver a power conversion efficiency (PCE) up to 16.2%. Notably, a high PCE up to $\sim 16\%$ can be secured for large-area devices (1.2 cm^2) with a SAM-modified ultrathin Ag electrode, which represents the highest performance ever reported for PeSCs with similar active areas. More significantly, the resulting devices also possess good ambient stability without the need for rigorous encapsulation.

Received 28th March 2016

Accepted 20th April 2016

DOI: 10.1039/c6ta02581a

www.rsc.org/MaterialsA

Introduction

Hybrid organic–inorganic lead halide perovskite solar cells (PeSCs) are considered to be a promising next-generation photovoltaic technology due to their potential for cost-effective manufacturing, light weight, and mechanical flexibility.^{1–5} The most widely studied perovskite material is methylammonium lead iodide (MAPbI₃), while formamidinium lead iodide (FAPbI₃) has attracted much attention very recently because of its superior properties such as a broad absorption range, high phase transition temperature, and superior stability.^{6–9} A dramatic increase in power conversion efficiency (PCE) of PeSCs has been achieved over the past few years, thanks to significant advances in improving the perovskite film quality and

engineering the interfacial properties between the active layer and the electrode.^{2–5} Ideally, the work-function (WF) of the cathode and anode must be aligned with the energy of the photo-excited quasi-Fermi levels of active layers to ensure ohmic contact for maximizing achievable open-circuit voltage (V_{oc}) and minimizing energy barriers for charge extraction without causing undesired bimolecular recombination.^{2–5} Typical approaches are to insert an interfacial layer to achieve appropriate energy level matching at the electrode-active layer interface.^{4,5,10}

In planar heterojunction PeSCs, a light absorbing perovskite layer is sandwiched between a hole transport layer (HTL) and an electron transport layer (ETL) that are in contact with their corresponding electrodes. Based on the direction of charge flow, the architectures of planar heterojunction PeSCs are categorized into the p–i–n and n–i–p configurations.³ Although PeSCs with the p–i–n configuration (substrate/anode/HTL/perovskite/ETL/cathode) have drawn much attention due to their low processing temperature and potential for use in plastic flexible devices,^{11–13} such devices generally have some inherent stability issues due mainly to the inclusion of hygroscopic and corrosive poly(3,4-ethylenedioxythiophene):poly(styrenesulfonate) (PEDOT:PSS) HTL and the easily oxidized low WF cathode metals (e.g. Al

^aDepartment of Materials Science and Engineering, Feng Chia University, Taichung, Taiwan 40724, Republic of China. E-mail: changcyu@fcu.edu.tw

^bInstitute of Nuclear Energy Research, Longtan, Taoyuan, Taiwan 32546, Republic of China

^cDepartment of Materials Science and Engineering, National Taiwan University, Taipei, Taiwan 10617, Republic of China

† Electronic supplementary information (ESI) available. See DOI: 10.1039/c6ta02581a

or Ca).^{14,15} To circumvent this problem, one can change the device architecture to the n-i-p configuration (substrate/cathode/ETL/perovskite/HTL/anode), where the transparent conductive electrode (e.g. indium tin oxide (ITO)) is covered with a cathode buffer layer (CBL) to form an effective electron selective contact with the ETL, whereas the original cathode is replaced with an environmentally stable high WF metal (e.g. Ag or Au) to collect holes.^{2,3} Very recently, a certified PCE of 20.1% was attained for PeSCs with the n-i-p configuration.⁶

CBL materials play an essential role in designing efficient and stable n-i-p PeSCs. n-Type metal oxides (e.g. TiO₂ or ZnO) have been considered as one of the best CBLs due to their solution processability, high optical transparency, good electrical properties, and appropriate energy levels.¹⁰ These oxides, however, generally require high-temperature annealing (>300 °C) for obtaining high quality high films,^{3,16} which obstructs the road towards the development of flexible devices and multi-junction tandem devices. Although recent efforts have been devoted to developing relatively low-temperature processing of metal oxide nanoparticle (NP) films as CBLs in PeSCs, the resulting performance is usually inferior to those of the devices with high-temperature processed metal oxide CBLs.^{11,17} In addition, these metal oxide-based devices usually suffer from severe hysteresis of photocurrent and interface-related degradations.^{5,18} Although organic-based compounds have been considered as viable alternative CBL materials in PeSCs, their susceptibility to degradation in the ambient atmosphere often raises stability concerns. To address this issue, a promising approach is to employ functional molecules that can be covalently bonded to the surface of the electrode.¹⁹ For example, decoration of the electrode surface with alkanethiol-based molecules has been proven to be an effective approach to tailor the interfacial properties while maintaining high stability.^{19–22} Recently, we have reported on an alkanethiol-based molecule (11-mercaptoundecyl)trimethyl-ammonium bromide (MUTAB) as an effective cathode buffer layer for PeSCs, and multiple positive effects on the interfaces can be observed, such as strong interface adhesion, good stability under a variety of conditions, and low contact resistance.²³ Despite these perceived advantages, this concept has rarely been applied to PeSCs so far.

On the other hand, despite impressive PCE values reported for PeSCs, these values have often been obtained for devices with relatively small active areas (<0.1 cm²). The significant performance deterioration (12–15% PCE) is usually observed when scaling from a champion device to a large-area device (active area > 1 cm²),^{24,25} due in part to the electrical loss of the commonly used transparent ITO electrode.²⁶ In addition, the scarcity of indium reserves can be a potential barrier to large-scale cost-effective manufacturing.^{20,27,28} ITO films are also poorly compatible with flexible substrates because they are prone to cracking upon bending, which presents a problem for flexible devices.^{20,27,28} These issues have motivated some attempts to prepare PeSCs without the use of ITO. Ideal transparent electrodes should possess high transparency, low sheet resistance, good stability, and low cost. Among new transparent electrode candidates, the ultrathin Ag film has emerged as a very promising alternative due to its extremely low resistance

and good transparency.^{20,28,29} In particular, the ultrathin Ag film is able to sustain low resistance even with high curvature stress without causing cracks, making it highly compatible with flexible devices.^{20,28,29} However, the development of ultrathin Ag films with both low resistance and high optical transmittance remains challenging, and this generally leads to the device performance far inferior to those of ITO-based devices.^{27,28,30} Considering the trade-off between transparency and conductivity, the film thickness of the ultrathin Ag layer is typically limited to be below 10 nm.^{28,29} Nevertheless, it is difficult to ensure that the as-grown film has good homogeneity and continuity at such a low thickness due mainly to the poor wettability of the Ag film on the substrate surface. The Ag films tend to form isolated islands on dielectric surfaces (Volmer-Weber growth mode), leading to a rough surface morphology with large grain sizes.^{31,32} The discrete Ag film can not only absorb and scatter light strongly (*i.e.*, low transparency) but also suffer from lack of conductive paths through the layer (*i.e.*, high electrical resistance).²⁸ The percolation threshold (*i.e.* the thickness corresponding to which the film morphology goes from island-like to continuous geometry) reported for Ag films is typically between 10 and 25 nm,³³ which in turn greatly compromises the optical transmittance. To improve the quality of ultrathin Ag films, an effective approach is to employ an adequate seed layer that can provide dense nucleation centers to reduce the percolation thickness and increase film uniformity at low thicknesses.^{20,34,35} Among various seed layer materials, alkanethiol-based self-assembled monolayers (SAMs) have gained considerable attention due to their ease of preparation and strong affinity for Ag atoms.^{20,36} The thiol moiety (–SH) on these molecules can react chemically with Ag and form a very stable Ag–S covalent bond.^{20,36} In addition, thiol-based SAMs are also compatible with patterning and large-scale production.¹⁹ Although this approach has been examined in organic-based electronic devices and great success has been achieved,^{20–22} its applicability in PeSCs has never been reported.

Recent studies have shown that modifying the substrate surface with SAMs can improve the morphology of perovskite layers and modulate the WF of the electrode, resulting in a substantial increase in device performance.^{37,38} In this study, for the first time, we demonstrate a facile and effective method to achieve high-performance and stable ITO-free PeSCs by the incorporation of thiol-functionalized SAM molecules 3-mercaptopropyltrimethoxysilane (MPTMS) and MUTAB to tailor the interfacial properties of the devices (see Fig. 1a for chemical structures). The device structure used herein is glass substrate/MPTMS SAM/ultrathin Ag/MUTAB SAM/PC₆₁BM/perovskite/poly[bis(4-phenyl)(2,4,6-trimethyl-phenyl)amine] (PTAA)/Ag, where MPTMS and MUTAB function as the seed layer for the ultrathin Ag film and CBL, respectively (see Fig. 1b). To evaluate the performance of our ITO-free devices, a control device with the structure of glass substrate/ITO/polyethyleneimine (PEI)/PC₆₁BM/perovskite/PTAA/Ag is also fabricated. The assembly of the MPTMS monolayer can be realized by the formation of covalent siloxane bonds through the condensation reaction between the hydrolyzed methoxysilane groups on MPTMS and native hydroxyl groups present at the substrate surface,^{39–41}

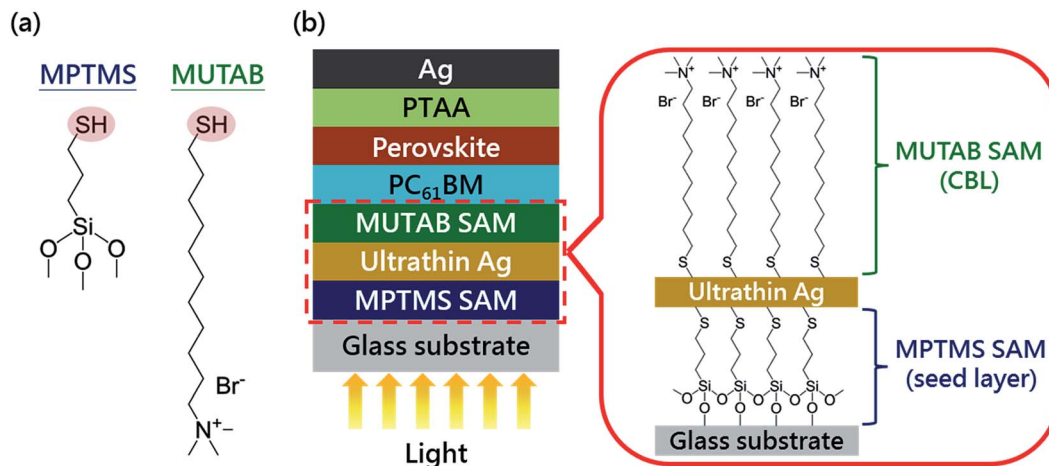


Fig. 1 (a) Chemical structures of SAM molecules. (b) Schematic illustration of the device architecture used in this study.

while the terminal thiol groups can interact with the incident Ag atoms and effectively lower the percolation thickness of the Ag layer to 8 nm, enabling the resulting film to exhibit an exceptionally low resistance of $\sim 6 \Omega \text{ sq}^{-1}$, high average transmittance (calculated between 380 and 750 nm) up to $\sim 78\%$, and good robustness against solvents and mechanical deformation. In addition to using the MPTMS SAM as the seed layer, the thiol groups on MUTAB can covalently bond to the Ag surface for SAM formation, while the terminal ammonium groups can induce the formation of favorable interfacial dipoles to turn a high-WF Ag electrode into an efficient low-WF electrode. With these improved interfacial properties, the resulting devices deliver a PCE up to 16.2%. In addition, the PCE remains high ($\sim 16\%$) for the devices with a larger active area (1.2 cm^2), greatly outperforming the ITO-based control devices ($\sim 13.4\%$). More significantly, the resulting devices possess good ambient stability without the need for rigorous encapsulation. The present findings imply that tailoring the atomic-scale interfacial properties plays an important role in the development of large-area PeSCs based on ultrathin Ag film transparent electrodes.

Results and discussion

First, the surface wettability of the glass substrate before and after modification with the MPTMS SAM was investigated by measuring the contact angle in a sessile water drop experiment. As shown in Fig. 2a, the contact angle on a cleaned glass substrate (*i.e.* without MPTMS SAM) was $\sim 15^\circ$. After MPTMS SAM modification, the surface became more hydrophobic, giving rise to a contact angle of $\sim 72^\circ$ (Fig. 2a). This value is in agreement with those previously reported for highly organized MPTMS SAM-modified surfaces,^{40–42} suggesting well-ordered structures with thiol groups pointing toward the free (air) surface. The high-resolution C 1s X-ray photoelectron spectroscopy (XPS) spectra were used to investigate the chemical bonding state of the samples before and after MPTMS SAM modification. As depicted in Fig. 2b, compared to the unmodified sample, the MPTMS SAM-modified sample exhibited

a more pronounced peak at $\sim 284.5 \text{ eV}$, corresponding to carbon bonded to silicon (C–Si) and hydrocarbon (C–C and C–H).⁴⁰ In addition, the peak assigned to carbon bonded to oxygen (C–O; $\sim 286.4 \text{ eV}$) was absent in the case of the MPTMS SAM-modified sample. These results imply that MPTMS molecules prefer to attach to the substrate surface for SAM formation, and the adverse effects such as physisorbed molecules and lateral cross-linking reactions between neighboring MPTMS molecules can be negligible. In addition, the thickness of MPTMS molecules on the surface was also estimated by ellipsometry, and the thickness was found to be $0.8 \pm 0.1 \text{ nm}$, which is close to the theoretical thickness of the MPTMS monolayer.^{40–42} The topographical atomic force microscopy (AFM) image of the MPTMS

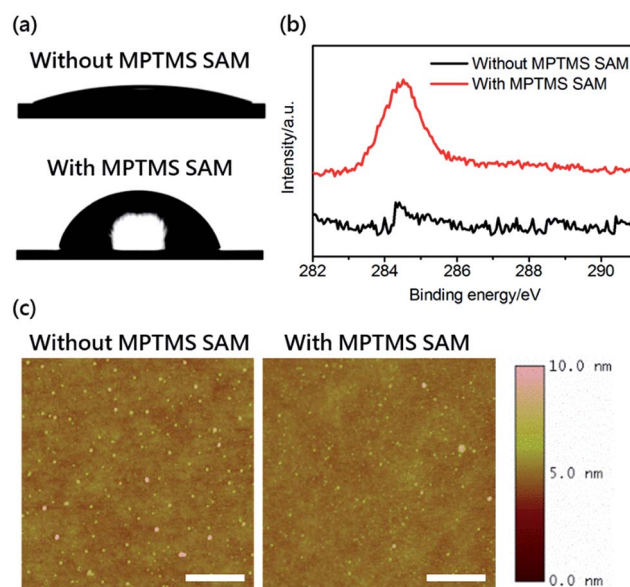


Fig. 2 (a) Images of water droplets on bare glass and MPTMS SAM-modified glass substrates. (b) XPS spectra of C 1s for bare glass and MPTMS SAM-modified glass substrates. (c) Topographical AFM images of bare glass and MPTMS SAM-modified glass substrates (scale bar = 500 nm).

SAM-modified surface revealed an extremely smooth surface with a room-mean-square (rms) surface roughness of ~ 0.5 nm, a value nearly identical to that measured for the unmodified surface (Fig. 2c), suggesting a comprehensive coverage of the monolayer film. These results suggest that the MPTMS SAM was successfully introduced onto the surface.

We then studied the influence of the MPTMS SAM on the electrical properties of ultrathin Ag films. The measurements were performed using a contactless measurement to assess the sheet resistances of Ag layers with different film thicknesses. For the Ag layer deposited without a MPTMS seed layer, a dramatic reduction of the sheet resistance was observed as the Ag thickness reached 12 nm (Fig. 3a), suggesting that 12 nm was the percolation threshold. While in the case of the film with the MPTMS SAM, a much lower percolation threshold of the Ag film was observed (8 nm; Fig. 3a). Encouragingly, the 8 nm Ag film delivered a remarkably low sheet resistance of $6.1 \Omega \text{ sq}^{-1}$, which is lower than that of the ITO layer ($\sim 20\text{--}50 \Omega \text{ sq}^{-1}$). The observed resistance differences could also be reflected in the morphological features of the films. The height and corresponding phase contrast images obtained by AFM for 8 nm Ag film growth on the bare and MPTMS SAM-coated substrates are shown in Fig. 3b–e. For the sample without the MPTMS SAM, a grainy structure with a rms surface roughness of ~ 4.3 nm was observed (Fig. 3b). Such grainy texture could also be manifested in the phase image (Fig. 3d). In contrast, the samples with MPTMS SAM modification revealed a relatively smooth and homogeneous surface morphology (rms roughness ~ 1.4 nm) with an unobservable phase contrast (Fig. 3c and e). The low percolation threshold of the Ag film obtained by employing the MPTMS SAM was also beneficial in improving the transmittance of the Ag layer. As depicted in Fig. 4a, the 8 nm Ag layer with MPTMS SAM modification showed an average transmittance of $\sim 67\%$, which was superior to that of the sample without the MPTMS SAM ($\sim 42\%$; see ESI Fig. S1[†]). Despite the considerable improvement in the optical transmittance, the obtained value of the MPTMS SAM-modified Ag layer was still lower than that of the ITO layer due in part to substantial portions of the incident light which were reflected by the ultrathin Ag layer, as shown in Fig. 4a. To address this issue, we employed a sol–gel zirconium oxide (ZrO_x) film as the anti-reflective (AR) coating to minimize the light reflection of the Ag layer (structure: glass substrate/

$\text{ZrO}_x/\text{MPTMS SAM}/8 \text{ nm Ag}$). ZrO_x was chosen because of its favorable optical characteristics (e.g. high refractive index, excellent transparency) and low-temperature solution processability (more details can be found in the Experimental part). As shown in Fig. 4a, the inclusion of ZrO_x AR coating (20 nm) could effectively lower the light reflection of the Ag layer and consequently improve the average transmittance to 78.2%, which was nearly comparable to that of the ITO layer (79.5%). The high optical transmittance of the transparent electrode is very advantageous for photon harvesting and photocurrent generation. It should be noted that the inclusion of ZrO_x AR coating did not apparently affect the electrical properties of the samples, as evidenced by the nearly identical resistance value of the AR-coated sample ($\sim 6.3 \Omega \text{ sq}^{-1}$) to that of the pristine sample. These results clearly indicate that the combination of the MPTMS seed layer and ZrO_x AR coating is very promising to promote the growth of dense and uniform ultrathin Ag films with low electrical resistance and high transmittance, making it highly suitable for transparent electrode applications.

To evaluate the robustness of MPTMS SAM-modified ultrathin Ag films (glass substrate/ $\text{ZrO}_x/\text{MPTMS SAM}/8 \text{ nm Ag}$), the films were subject to ultrasonic agitation (20 min) with the solvents used for substrate cleaning procedures (i.e. DI water, acetone, and isopropanol). Notably, the resulting films exhibited exceptional robustness: the sheet resistance remained essentially unchanged (Fig. 4b). In contrast, the resistance value of the Ag layer without the MPTMS SAM became immeasurable after these procedures. This difference could be ascribed to good interfacial adhesion between the MPTMS SAM and Ag layer. Another important aspect associated with the ultrathin Ag film is its mechanical stability (i.e., the endurance of electrical properties under continuous bending stress conditions). Here, the MPTMS SAM-modified Ag layer on a polyethylene terephthalate (PET) substrate (structure: PET/ $\text{ZrO}_x/\text{MPTMS SAM}/8 \text{ nm Ag}$) was bent to a cylinder (radius of curvature = 5 mm), and its sheet resistance was then investigated after intensively repeated bending cycles. The commercially available ITO-coated PET substrate was also used for comparison. As shown in Fig. 4c, after 1000 bending cycles, the sample retained its low resistance ($\sim 6.7 \Omega \text{ sq}^{-1}$), suggesting its potential application in flexible electronics. In contrast, the resistance value of the ITO-coated PET substrate deteriorated rapidly after repeated bending (Fig. 4c), possibly due to the formation of cracks in the ITO film. It should be mentioned that the average transmittance of this MPTMS SAM-modified Ag layer on the PET substrate still remains high ($\sim 76\%$), as shown in ESI Fig. S2[†]. The photographic images of this sample are shown in Fig. 4d, where the campus building and logo can be visualized clearly through the sample. These results show that the MPTMS SAM-modified Ag layer exhibits exceptional robustness under ultrasonic agitation in common solvents and great tolerance to severe deformations. We envisage that such a SAM-modified Ag layer is potentially applicable for devices that require stable and flexible electrodes, and this is the subject of our ongoing research.

To examine the applicability of the newly developed ultrathin Ag layer as the transparent electrode in PeSCs, the photovoltaic performance of the device with the structure of glass

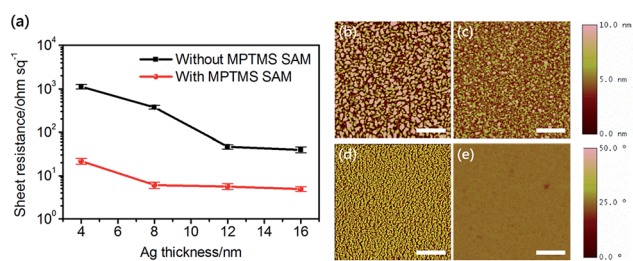


Fig. 3 (a) Thickness dependence of sheet resistance of Ag films with and without the bottom MPTMS SAM. AFM topographic (upper row) and phase (lower row) images of 8 nm Ag films: (b and d) without the bottom MPTMS SAM, (c and e) with the bottom MPTMS SAM. The scale bar in each panel is 500 nm.

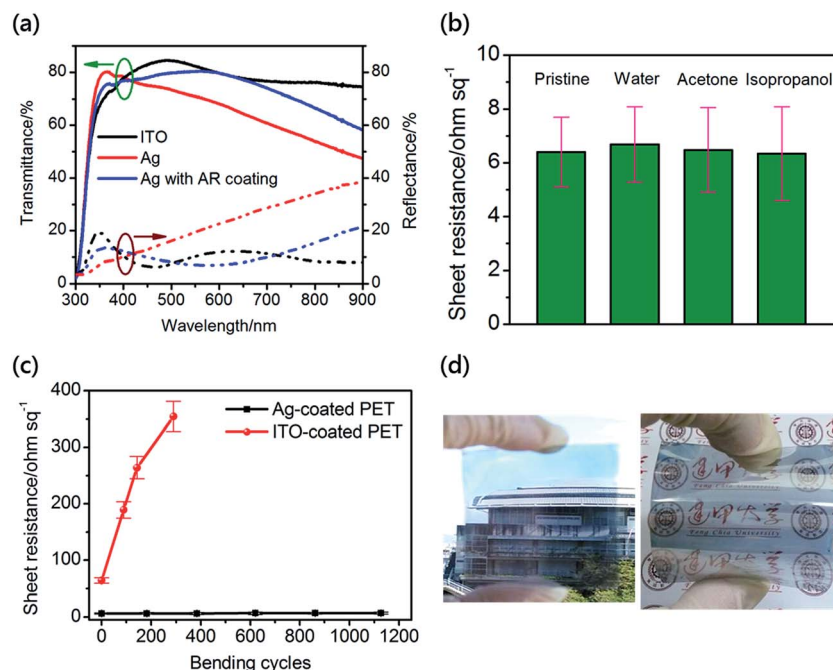


Fig. 4 (a) Optical transmittance and reflectance spectra of the transparent electrode studied in this work. (b) Sheet resistance of MPTMS SAM/8 nm Ag films before and after ultrasonic agitation in three common solvents (water, acetone, and isopropanol); the statistical data were collected from more than 20 samples. (c) Sheet resistance of ITO-coated PET and MPTMS SAM/8 nm Ag-coated PET as a function of bending cycles; the statistical data were collected from more than 10 samples. (d) Photographs of MPTMS SAM/8 nm Ag-coated PET samples.

substrate/ZrO_x/MPTMS SAM/Ag (8 nm)/PC₆₁BM/MAPbI₃/PTAA/Ag was measured. A control device with an ITO electrode was also fabricated for comparison. The MAPbI₃ perovskite film was prepared by two-step sequential solution deposition, and its detailed characterization can be found in our previous studies.^{23,43–45} The solar-to-electrical PCE was evaluated by recording the current–voltage (*J*–*V*) characteristics under simulated AM 1.5 G conditions (intensity = 100 mW cm⁻²). The average values and the corresponding standard deviations of photovoltaic parameters including *V*_{oc}, short-circuit current density (*J*_{sc}), fill factor (FF), and PCE are summarized in Table 1. The *J*–*V* characteristics of the best performing devices are also depicted in Fig. 5a, and the detailed photovoltaic parameters are listed in Table 1. For the control device employing the ITO electrode (device A), an average PCE of 14.30% was attained, with a *J*_{sc} of 20.13 mA cm⁻², *V*_{oc} of 1.00 V, and FF of 71.15% (Table 1). The obtained PCE values are comparable to the optimal device characteristics reported by other researchers for

the same device structure.⁴⁶ When using ultrathin Ag as the transparent electrode (device B), however, it failed to show expected high photovoltaic efficiencies. As shown in Table 1, device B exhibited an average PCE of 1.23%, with a *J*_{sc} of 10.36 mA cm⁻², *V*_{oc} of 0.38 V, and FF of 31.50%. This inferior PCE can be rationalized by the fact that a large energy barrier exists between the LUMO level of PC₆₁BM (~4.1 eV) and the WF of Ag (~4.7 eV),^{23,43–45,47,48} thus impeding efficient extraction of electrons, as depicted in Fig. 6a.

To adjust the mismatch of the energy level between the PC₆₁BM layer and Ag electrode, we employed MUTAB as the interfacial modification layer. MUTAB decorated with thiol end-groups can form a SAM on the Ag surface *via* the formation of a stable Ag–S covalent bond. On the other hand, the ammonium cations on the MUTAB SAM are expected to have positive effects on WF modulation of the Ag layer, as the ammonium cations have been proven to interact strongly with the electrode surface and thus form favorable interfacial dipoles toward the active

Table 1 Summary of the photovoltaic properties of MAPbI₃-based devices. The values in parenthesis are for the best performing devices

Device	Electrode/CBL	<i>V</i> _{oc} [volt]	<i>J</i> _{sc} [mA cm ⁻²]	FF [%]	PCE [%]
A ^a	ITO/PEI	1.00 ± 0.01 (1.01)	20.13 ± 0.64 (21.04)	71.15 ± 4.13 (72.05)	14.30 ± 0.61 (15.31)
B ^b	Ag	0.38 ± 0.01 (0.37)	10.36 ± 1.05 (10.20)	31.50 ± 4.57 (36.57)	1.23 ± 0.10 (1.38)
C ^a	Ag/MUTAB SAM ^c	1.00 ± 0.01 (1.00)	19.99 ± 0.74 (19.76)	72.72 ± 3.54 (76.57)	14.48 ± 0.64 (15.13)
D ^a	Ag/MUTAB SAM ^d	1.00 ± 0.01 (1.01)	16.42 ± 0.90 (17.32)	74.36 ± 4.39 (73.94)	12.13 ± 0.55 (12.93)

^a Average and standard deviation values were obtained based on 50 devices. ^b Average and standard deviation values were obtained based on 20 devices. ^c With ZrO_x AR coating. ^d Without ZrO_x AR coating.

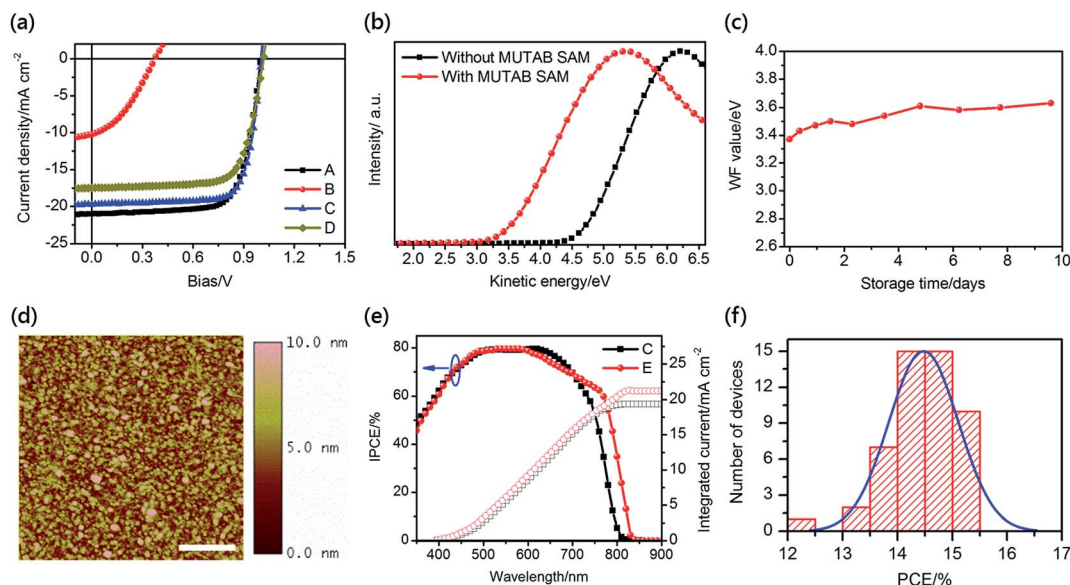


Fig. 5 (a) J - V characteristics of the best performing MAPbI₃-based devices under simulated AM 1.5 solar irradiation (intensity = 100 mW cm⁻²). (b) UPS spectra of bare Ag and MUTAB SAM-modified Ag layers. (c) Evolution of the WF of MUTAB SAM-modified Ag layer as a function of storage time in air. (d) Topographical AFM image of the MUTAB SAM-modified Ag film (scale bar = 500 nm). (e) IPCE and integrated current spectra of the as-fabricated devices (devices C and E for MAPbI₃ and FAPbI₃ system, respectively). (f) Histogram of solar cell efficiencies (device C) for 50 devices.

layer, leading to a significant increase of the vacuum level of the electrode for efficient electron extraction.^{23,44,45,47,48} To confirm this, the WF of the Ag layer before and after modification with the MUTAB SAM was determined by ultraviolet photoelectron spectroscopy (UPS) measurements. As shown in Fig. 5b, the WF value of the bare Ag layer was determined to be 4.67 eV, which is consistent with the reported results.^{47,48} When the Ag layer was modified with the MUTAB SAM, the WF was reduced to 3.35 eV (Fig. 5b). The low WF contact at the cathode interface can lead to better energy level matching with the PC₆₁BM layer (Fig. 6b), which is beneficial for efficient electron extraction.¹⁰ It should be noted that long alkyl chains of MUTAB can deliver several advantages such as high solubility in a wide range of solvents and high robustness in SAM applications, as described previously.^{19,49} The stability of the MUTAB SAM-modified Ag sample was also examined by investigating the WF evolution of the

samples as a function of exposure time to ambient conditions (30 °C, ~60% relative humidity). Encouragingly, the sample was found to be fairly stable, as the change in WF was nearly negligible after more than 200 h of exposure (Fig. 5c). In addition to providing appropriate energy alignment, the interfacial morphology also plays an important role in determining device performance. The surface morphology of the deposited film was investigated by AFM. The MUTAB SAM-modified Ag film exhibited a smooth and homogenous morphology with a rms roughness of ~1.6 nm (Fig. 5d), which could lead to good interfacial contact and consequently high device performance. These results provide solid evidence that the modification of the ultrathin Ag surface with the MUTAB SAM can considerably lower the WF value to facilitate electron extraction.

When applying the MUTAB SAM to the devices (structure: glass substrate/ZrO_x/MPTMS SAM/Ag/MUTAB SAM/PC₆₁BM/

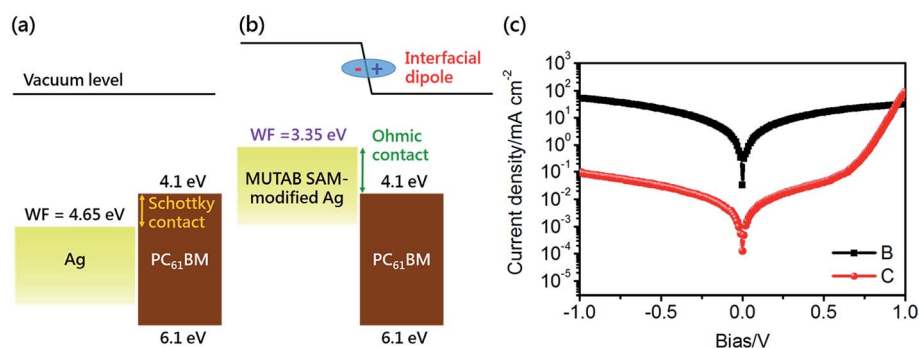


Fig. 6 Energy level diagram at the active layer/cathode interface: (a) without the MUTAB SAM and (b) with MUTAB SAM. (c) Dark J - V characteristics of the as-fabricated devices.

MAPbI₃/PTAA/Ag; device C), a substantial improvement in PCE (by ~12 fold) was observed as a result of the simultaneous increase of all the parameters. As shown in Table 1, device C exhibited an average PCE of 14.48%, with a J_{sc} of 19.99 mA cm⁻², V_{oc} of 1.00 V, and FF of 72.72%. In particular, the best performing device showed a PCE of 15.13%, with a J_{sc} of 19.76 mA cm⁻², V_{oc} of 1.00 V, and FF of 76.57% (Table 1 and Fig. 5a). To evaluate the accuracy of the photovoltaic results, the J_{sc} values were calculated from integration of incident photon-to-current conversion efficiency (IPCE) spectra with the AM 1.5 G reference spectrum. The calculated J_{sc} agreed very well with the measured J_{sc} values (within 10% error), as shown in Table 1 and Fig. 5e. In addition, the obtained device performance of ultrathin Ag-based devices was comparable to that of ITO-based devices (Table 1 and Fig. 5a), clearly indicating the effectiveness of using MPTMS and MUTAB SAMs as promising interfacial materials in ITO-free PeSCs. To examine the reproducibility of the devices, a histogram of device performance obtained from 50 samples of device C is summarized in Fig. 5f. Importantly, more than 80% of the integrated devices delivered PCE above 14% with low standard deviation (Table 1 and Fig. 6f), indicating good reproducibility. This could be associated with superior contact properties between SAMs and Ag layers as discussed previously. It should be noted that the performance of the devices without ZrO_x AR coating (device D) was inferior to that of device C (Table 1 and Fig. 5a) mainly because of lower J_{sc} values, which was in good agreement with the transmittance spectrum (Fig. 4a). These results confirmed the necessity and effectiveness of the MUTAB SAM and AR coating in PeSCs with ultrathin Ag transparent electrodes.

To shed light on the origin behind the performance enhancement of MUTAB SAM-modified devices, the series resistance (R_s) and shunt resistance (R_{sh}) of the devices were investigated. The R_s and R_{sh} are calculated from the inverse slope of the J - V characteristics under dark conditions close to 0 and 1 V, respectively. As shown in ESI Table S1† and Fig. 6c, compared to the device without the MUTAB SAM (device A), the device with MUTAB SAM modification (device C) exhibited an improved rectification ratio with lower series resistance and higher shunt resistance (*i.e.* less charge recombination and leakage current), indicating more effective charge selective contact.¹⁰ These results elucidate that the MUTAB SAM can provide interfacial modification superior to that of the unmodified sample, ensuring efficient electron extraction and preventing undesirable electron-hole recombination at the interface between the active layer and Ag electrode.

The universality of the proposed approach in PeSCs was examined by employing FAPbI₃ perovskite as the photoactive layer, which is potentially superior to conventional MAPbI₃ as the light harvester due to its smaller bandgap.⁶⁻⁹ The preparation and detailed characterization of FAPbI₃ perovskite films can be found in our previous work.⁴⁵ The device fabrication was the same as that for MAPbI₃-based devices, except that the photoactive layer was replaced by FAPbI₃ (see Experimental for details). The J - V characteristics of the best performing devices are shown in Fig. 7a, and the detailed photovoltaic parameters are summarized in Table 2. Very encouragingly, the best

performing device (device E) delivered a remarkable PCE of 16.23%, with a J_{sc} of 22.84 mA cm⁻², V_{oc} of 1.00 V, and FF of 70.34% (Table 2 and Fig. 7a). It should be emphasized again that the obtained PCE was comparable to those of the devices based on the ITO electrode (device F; maximum PCE = 16.5%), as shown in Table 2 and Fig. 7a. Note that the measured J_{sc} of device E agreed very well (within 10% error) with the J_{sc} value integrated from the IPCE spectrum (Fig. 5e), which confirmed the accuracy of our reported PCE value. A good stabilized power output was also observed for device E, delivering a steady-state PCE value as high as 16.80% under continuous illumination (Fig. 7b). It should be emphasized again that all key parameters of the device with SAM modification (device E) were highly reproducible with low standard deviation (Table 2). A histogram of device performance obtained from 50 samples of device E is also presented in Fig. 7c, and more than 50% of the integrated devices delivered PCE above 15%. In addition, given that planar heterojunction PeSCs have been shown to be prone to hysteresis,^{2,3} J - V characteristics of the devices (device E) measured under different scan directions and various voltage sweep rates were then analyzed. Encouragingly, our device exhibited photocurrent hysteresis-less J - V characteristics with different scanning directions and/or voltage sweep rates (ESI Fig. S3†), which can be explained by the use of appropriate charge selective contact layers and/or stable formamidinium cations in the FAPbI₃ perovskite structure under the electric field.^{6,9} These results provide strong evidence of the general utility of MPTMS and MUTAB SAM modification in PeSCs.

The applicability of this concept to large-area ITO-free PeSCs was also examined. As a proof of concept, we fabricated the devices with larger active areas of 1.2 or 5.04 cm². The fabrication procedure and device structure were the same as those for the small-area devices (device E) except for the active area. For the devices with 1.2 cm² active area (device G), the best PCE reached 15.98%, with a J_{sc} of 21.68 mA cm⁻², V_{oc} of 0.99 V, and FF of 71.58% (Table 2 and Fig. 7a). Notably, the obtained PCE of device G greatly outperformed that of the control device using the ITO electrode (device H; PCE = 13.36%), as shown in Table 2 and Fig. 7a. This improvement can be ascribed to the fact that the ultrathin Ag layer possessed a much lower electrical resistance than the widely used ITO layer, as we have investigated previously. It should be noted that 15.98% PCE is among one of the highest reported values for PeSCs with similar active areas (~1.0 cm²).^{45,50} More encouragingly, a reasonable PCE of 12.79% was also attained for the devices with a larger active area of 5.04 cm² (device I; see Table 2 and Fig. 7a), and a stabilized power output at a PCE of 12.75% was observed (Fig. 7b). A photographic image of device I is shown in the inset of Fig. 7b. The remarkable device performance can be ascribed to the superior interfacial properties afforded by MPTMS and MUTAB SAMs. Given that organic-inorganic lead halide perovskite materials will decompose rapidly in the presence of moisture,^{51,52} the shelf stability of large-area FAPbI₃-based devices (device G) was also examined by monitoring the evolution of their PCEs as a function of time during storage under ambient conditions (30 °C, ~60% relative humidity). In our case, no extra package or encapsulation layer was used. Notably, after being exposed to

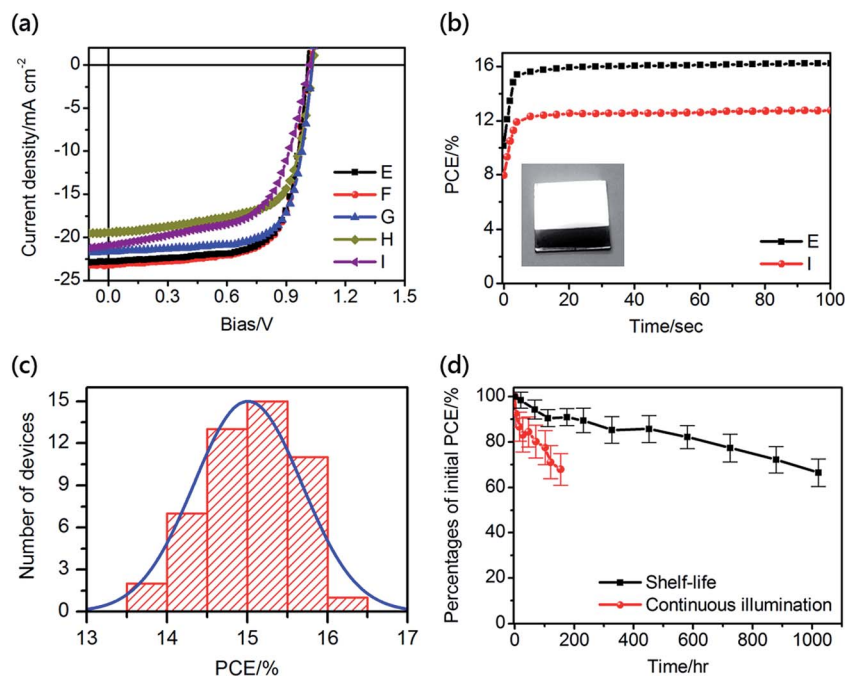


Fig. 7 (a) J - V characteristics of the best performing FAPbI₃-based devices under simulated AM 1.5 solar irradiation (intensity = 100 mW cm⁻²). (b) Stabilized power output measured close to the maximum power point (~0.9 V) for devices E and I. The inset shows a photograph of device I. (c) Histogram of solar cell efficiencies (device E) for 50 devices. (d) Degradation profile of device G as a function of storage time in air; the statistical data were collected from more than 30 devices.

Table 2 Summary of the photovoltaic properties of FAPbI₃-based devices. The values in parenthesis are for the best performing devices

Device	Electrode/CBL	V_{oc} [volt]	J_{sc} [mA cm ⁻²]	FF [%]	PCE [%]
E ^a	Ag/MUTAB SAM ^b	1.00 ± 0.01 (1.01)	21.04 ± 0.75 (22.84)	71.62 ± 3.60 (70.34)	15.01 ± 0.67 (16.23)
F ^a	ITO/PEI ^b	1.00 ± 0.01 (1.01)	22.73 ± 0.71 (23.16)	66.52 ± 3.96 (70.54)	15.11 ± 0.68 (16.50)
G ^c	Ag/MUTAB SAM ^d	0.99 ± 0.01 (1.03)	21.32 ± 1.12 (21.68)	70.35 ± 4.23 (71.58)	14.87 ± 0.55 (15.98)
H ^c	ITO/PEI ^d	1.00 ± 0.01 (1.02)	21.25 ± 1.17 (19.43)	58.23 ± 4.73 (67.41)	12.25 ± 0.62 (13.36)
I ^c	Ag/MUTAB SAM ^e	1.00 ± 0.01 (1.03)	20.17 ± 0.91 (20.94)	57.43 ± 4.59 (59.28)	11.81 ± 0.67 (12.79)

^a Average and standard deviation values were obtained based on 50 devices. ^b Active area = 0.12 cm². ^c Average and standard deviation values were obtained based on 30 devices. ^d Active area = 1.2 cm². ^e Active area = 5.04 cm².

more than 1000 h, over 65% of the initial PCE could be retained for these devices (Fig. 7d). This might be due to the use of a hydrophobic tetrafluoro-tetracyanoquinodimethane (F4TCNQ)-doped HTL and environmentally stable Ag electrode, which has shown to successfully improve the stability of the perovskite layer.^{53,54} In particular, we found that these devices remained fairly stable under continuous light illumination (intensity = 100 mW cm⁻²) in an ambient atmosphere: ~70% of the initial efficiency was retained over 150 h continuous testing (Fig. 7d), demonstrating good stability of our devices. We suggest that the inferior stability of the devices under continuous light illumination may be associated with photoinduced degradation and/or insufficient thermal stability of the materials (*e.g.* PC₆₁BM or perovskite layers).^{51,52} These results clearly elucidate the high compatibility of MPTMS and MUTAB SAMs with scale-up fabrication, enabling the resulting devices to exhibit both high performance and good stability.

Conclusions

We have demonstrated a facile and effective method to improve the performance and stability of ITO-free perovskite solar cells by the incorporation of thiol-functionalized SAMs MPTMS and MUTAB as the seed layer for an ultrathin Ag film and CBL, respectively. The MPTMS SAM can effectively modify the Ag growth kinetics and reduce the percolation threshold of the ultrathin Ag layer to 8 nm, enabling the resulting film to exhibit a smooth surface morphology, exceptional low sheet resistance (6.1 Ω sq⁻¹), high average transmittance (~78%), and high robustness against solvents and mechanical deformation. These characteristics, especially in terms of electrical resistance and mechanical flexibility, are much superior to those of the state-of-the-art ITO film. Besides using the MPTMS SAM as the seed layer, the MUTAB SAM can induce the formation of

favorable interfacial dipoles to tailor the WF of the Ag layer, allowing the use of a high work function Ag layer as an effective cathode. With these desired interfacial properties, the resulting devices deliver a PCE up to 16.2%. Importantly, the large-area devices (1.2 cm²) with a SAM-modified ultrathin Ag electrode deliver a record-high PCE of ~16% for PeSCs with similar active areas. More significantly, the resulting devices possess good ambient stability without the need for rigorous encapsulation. This work is an excellent example of employing SAMs to achieve highly efficient and stable ITO-free PeSCs, and the approach demonstrated herein is especially valuable for the development of large-area devices.

Experimental

Materials

Patterned ITO-coated glass substrates with a sheet resistance of 15 ohm sq⁻¹ were purchased from Ruilong Tech. PC₆₁BM (>99.5%) was purchased from Solenne. Methylammonium iodide (MAI; >99.5%) and formamidinium iodide (FAI; >99.5%) were purchased from Lumtec. For preparation of a lead iodide (PbI₂) complex, 25 g PbI₂ was dissolved in anhydrous dimethylsulfoxide (DMSO) of 75 mL and toluene of 200 mL was then slowly added into the PbI₂ solution. The white precipitate was then filtered and dried in a vacuum oven at 60 °C for 12 h. Unless otherwise stated, all chemicals were purchased from Sigma-Aldrich and used as received.

ZrO_x film preparation

A ZrO_x film (20 nm) was formed by spin-coating precursor solution on top of the cleaned substrates (6000 rpm for 60 s), followed by curing under a high-pressure mercury UV lamp (intensity = 180 mW cm⁻²) for 3 h under ambient conditions (30 °C, ~60% relative humidity) to densify the film without the need for high-temperature thermal annealing.

Preparation of SAM-modified ultrathin Ag films

The substrates were cleaned stepwise in detergent, water, acetone, and isopropyl alcohol under ultra-sonication for 20 min each and subsequently pretreated with UV-ozone for 60 min. The substrates were transferred to a nitrogen-filled glovebox and immersed in 60 mM MPTMS toluene solution for 12 h. After removing from the solutions, the substrates were rinsed with toluene and blown dry with nitrogen. The deposition of ultrathin Ag films on these substrates, with and without the MPTMS SAM, was carried out by vacuum evaporation under high vacuum (<10⁻⁶ torr) with a deposition rate of 0.5 nm s⁻¹. The Ag thickness was measured using a carefully calibrated quartz-crystal microbalance mounted adjacent to the substrates. The substrates were then transferred to a nitrogen-filled glovebox and immersed in 30 mM MUTAB DMSO solution for 6 h. After removing from the solutions, the substrates were rinsed with DMSO and blown dry with nitrogen.

Solar cell fabrication

For the devices with SAM-modified ultrathin Ag films, a PC₆₁BM layer (40 nm) was cast by spin-coating a PC₆₁BM solution (20 mg mL⁻¹ in chlorobenzene; 1000 rpm for 60 s) on top of the SAM-modified ultrathin Ag layers. For MAPbI₃-based devices, a MAPbI₃ perovskite layer (~380 nm) was prepared following two-step solution deposition, as described in our previous work.^{23,43–45} Briefly, lead iodide (PbI₂) and methyl ammonium iodide (MAI) were dissolved in DMF and 2-propanol with concentrations of 450 mg mL⁻¹ for PbI₂ and 40 mg mL⁻¹ for MAI, respectively. Both solutions and substrates were heated at 100 °C for 10 min before being used. A PbI₂ solution was spun on a preheated substrate (5000 rpm for 40 s) and then annealed at 70 °C for 10 min. The MAI solution was then spun on top of the dried PbI₂ film (6000 rpm for 30 s), followed by annealing at 100 °C for 2 h. For FAPbI₃-based devices, a FAPbI₃ perovskite layer (~320 nm) was prepared according to the reported procedure.^{6,45} Briefly, a PbI₂ complex solution (1.3 M in anhydrous DMF) was spun on the substrate (3000 rpm for 30 s). A FAI solution (0.465 M in anhydrous 2-propanol) was then spun on top of the dried PbI₂ complex film (5000 rpm for 30 s), followed by annealing at 150 °C for 10 min. Afterward, a PTAA layer (80 nm; 3000 rpm for 60 s) was then spin-coated on top of the formed perovskite layers from a solution of PTAA (15 mg mL⁻¹ in toluene) with the addition of 1 wt% F4TCNQ dopant. The opaque Ag (150 nm) was then deposited from a thermal evaporator under high vacuum (<10⁻⁶ torr). Contributions to the *J*_{sc} from regions outside the active area were eliminated using illumination masks with aperture sizes of 0.12 cm², 1.2 cm², or 5.04 cm². The ITO-based control devices were fabricated following the same procedure presented above except that the CBL was replaced with a PEI layer (10 nm). Briefly, a PEI layer was spin-coated on patterned ITO glass substrates from PEI solution (2 mg mL⁻¹ in 2-methoxyethanol; 5000 rpm 60 s), followed by annealing at 110 °C for 20 min.

Characterization

The current–voltage characteristics of the as-fabricated solar cells were measured under ambient conditions using a Keithley 2400 source measurement unit. Unless otherwise stated, the scan rate was set at 0.15 V s⁻¹. An Oriel xenon lamp (450 Watt) with an AM1.5 G filter was used as the solar simulator. A Hamamatsu silicon solar cell with a KG5 color filter, which is traced to the National Renewable Energy Laboratory (NREL), was used as the reference cell. To calibrate the light intensity of the solar simulator, the power of the xenon lamp was adjusted to make the *J*_{sc} of the reference cell under simulated sun light as high as it was under the calibration condition. IPCE spectra were measured using a lock-in amplifier with a current preamplifier under short-circuit conditions with illumination of monochromatic light from a 250 W quartz-halogen lamp (Osram) passing through a monochromator. The optical measurements were performed with a JASCO V-670 UV-Vis spectrometer. The work functions of the electrodes were measured with a ULVAC-PHI PHI 5000 Versaprobe II X-ray photoelectron spectrometer employing a monochromatic

focused Al-K α X-ray source and a hemispherical analyzer. The high-resolution of C 1s spectra were recorded in a XPS spectrometer (Thermo Scientific) with a monochromatic Al K-alpha X-ray source (1486.6 eV). The resistance of the thin films was measured by using a four point probe setup with a source measurement unit (Keithley 2400). The surface morphology of the films was studied using a tapping mode AFM from Digital Instrument D3100CL. The electrical conductivities of the thin films were measured by using a four point probe setup with a source measurement unit (Keithley 2400).

Acknowledgements

The authors acknowledge the support from the Ministry of Science and Technology (MOST 04-2221-E-035-035 and 104-2119-M-009-012). The authors appreciate the Precision Instrument Support Center of Feng Chia University for providing the fabrication and measurement facilities.

Notes and references

- M. Liu, M. B. Johnston and H. J. Snaith, *Nature*, 2013, **501**, 395–398.
- P. Gao, M. Gratzel and M. K. Nazeeruddin, *Energy Environ. Sci.*, 2014, **7**, 2448–2463.
- H. S. Jung and N.-G. Park, *Small*, 2015, **11**, 10–25.
- O. Malinkiewicz, A. Yella, Y. H. Lee, G. M. Espallargas, M. Graetzel, M. K. Nazeeruddin and H. J. Bolink, *Nat. Photonics*, 2014, **8**, 128–132.
- H. Zhou, Q. Chen, G. Li, S. Luo, T.-b. Song, H.-S. Duan, Z. Hong, J. You, Y. Liu and Y. Yang, *Science*, 2014, **345**, 542–546.
- W. S. Yang, J. H. Noh, N. J. Jeon, Y. C. Kim, S. Ryu, J. Seo and S. I. Seok, *Science*, 2015, **348**, 1234–1237.
- S. Pang, H. Hu, J. Zhang, S. Lv, Y. Yu, F. Wei, T. Qin, H. Xu, Z. Liu and G. Cui, *Chem. Mater.*, 2014, **26**, 1485–1491.
- G. E. Eperon, S. D. Stranks, C. Menelaou, M. B. Johnston, L. M. Herz and H. J. Snaith, *Energy Environ. Sci.*, 2014, **7**, 982–988.
- J.-W. Lee, D.-J. Seol, A.-N. Cho and N.-G. Park, *Adv. Mater.*, 2014, **26**, 4991–4998.
- C.-C. Chueh, C.-Z. Li and A. K. Y. Jen, *Energy Environ. Sci.*, 2015, **8**, 1160–1189.
- J. You, Z. Hong, Y. Yang, Q. Chen, M. Cai, T.-B. Song, C.-C. Chen, S. Lu, Y. Liu, H. Zhou and Y. Yang, *ACS Nano*, 2014, **8**, 1674–1680.
- L. Meng, J. You, T.-F. Guo and Y. Yang, *Acc. Chem. Res.*, 2016, **49**, 155–165.
- P. Docampo, J. M. Ball, M. Darwich, G. E. Eperon and H. J. Snaith, *Nat. Commun.*, 2013, **4**, 2761.
- A. Guerrero, J. You, C. Aranda, Y. S. Kang, G. Garcia-Belmonte, H. Zhou, J. Bisquert and Y. Yang, *ACS Nano*, 2016, **10**, 218–224.
- T. A. Berhe, W.-N. Su, C.-H. Chen, C.-J. Pan, J.-H. Cheng, H.-M. Chen, M.-C. Tsai, L.-Y. Chen, A. A. Dubale and B.-J. Hwang, *Energy Environ. Sci.*, 2016, **9**, 323–356.
- N. J. Jeon, H. G. Lee, Y. C. Kim, J. Seo, J. H. Noh, J. Lee and S. I. Seok, *J. Am. Chem. Soc.*, 2014, **136**, 7837–7840.
- H. Zhou, Y. Shi, K. Wang, Q. Dong, X. Bai, Y. Xing, Y. Du and T. Ma, *J. Phys. Chem. C*, 2015, **119**, 4600–4605.
- Y. Cheng, Q.-D. Yang, J. Xiao, Q. Xue, H.-W. Li, Z. Guan, H.-L. Yip and S.-W. Tsang, *ACS Appl. Mater. Interfaces*, 2015, **7**, 19986–19993.
- J. C. Love, L. A. Estroff, J. K. Kriebel, R. G. Nuzzo and G. M. Whitesides, *Chem. Rev.*, 2005, **105**, 1103–1170.
- J. Zou, C.-Z. Li, C.-Y. Chang, H.-L. Yip and A. K. Y. Jen, *Adv. Mater.*, 2014, **26**, 3618–3623.
- J. H. Cho, J. A. Lim, J. T. Han, H. W. Jang, J.-L. Lee and K. Cho, *Appl. Phys. Lett.*, 2005, **86**, 171906.
- H.-L. Yip, S. K. Hau, N. S. Baek and A. K.-Y. Jen, *Appl. Phys. Lett.*, 2008, **92**, 193313.
- C.-Y. Chang, Y.-C. Chang, W.-K. Huang, K.-T. Lee, A.-C. Cho and C.-C. Hsu, *Chem. Mater.*, 2015, **27**, 7119–7127.
- W. Chen, Y. Wu, Y. Yue, J. Liu, W. Zhang, X. Yang, H. Chen, E. Bi, I. Ashraful, M. Grätzel and L. Han, *Science*, 2015, **350**, 944–948.
- S. Bai, Z. Wu, X. Wu, Y. Jin, N. Zhao, Z. Chen, Q. Mei, X. Wang, Z. Ye, T. Song, R. Liu, S.-t. Lee and B. Sun, *Nano Res.*, 2014, **7**, 1749–1758.
- J. D. Servaites, S. Yeganeh, T. J. Marks and M. A. Ratner, *Adv. Funct. Mater.*, 2010, **20**, 97–104.
- N. Formica, P. Mantilla-Perez, D. S. Ghosh, D. Janner, T. L. Chen, M. Huang, S. Garner, J. Martorell and V. Pruneri, *ACS Appl. Mater. Interfaces*, 2015, **7**, 4541–4548.
- I. Lee and J.-L. Lee, *J. Photonics Energy*, 2015, **5**, 057609.
- H. Kang, S. Jung, S. Jeong, G. Kim and K. Lee, *Nat. Commun.*, 2015, **6**, 6503.
- H. W. Choi, N. D. Theodore and T. L. Alford, *Sol. Energy Mater. Sol. Cells*, 2013, **117**, 446–450.
- M. Hu, S. Noda and H. Komiyama, *Surf. Sci.*, 2002, **513**, 530–538.
- C. T. Campbell, *Surf. Sci. Rep.*, 1997, **27**, 1–111.
- R. S. Sennett and G. D. Scott, *J. Opt. Soc. Am.*, 1950, **40**, 203–210.
- S. Schubert, J. Meiss, L. Müller-Meskamp and K. Leo, *Adv. Energy Mater.*, 2013, **3**, 438–443.
- S. Schubert, M. Hermenau, J. Meiss, L. Müller-Meskamp and K. Leo, *Adv. Funct. Mater.*, 2012, **22**, 4993–4999.
- T. Fudei, M. Kawamura, Y. Abe and K. Sasaki, *J. Nanosci. Nanotechnol.*, 2012, **12**, 1188–1191.
- L. Zuo, Z. Gu, T. Ye, W. Fu, G. Wu, H. Li and H. Chen, *J. Am. Chem. Soc.*, 2015, **137**, 2674–2679.
- Z. Gu, L. Zuo, T. T. Larsen-Olsen, T. Ye, G. Wu, F. C. Krebs and H. Chen, *J. Mater. Chem. A*, 2015, **3**, 24254–24260.
- C. Haensch, S. Hoepfner and U. S. Schubert, *Chem. Soc. Rev.*, 2010, **39**, 2323–2334.
- M. Hu, S. Noda, T. Okubo, Y. Yamaguchi and H. Komiyama, *Appl. Surf. Sci.*, 2001, **181**, 307–316.
- E. Pavlovic, A. P. Quist, U. Gelius and S. Oscarsson, *J. Colloid Interface Sci.*, 2002, **254**, 200–203.
- D. K. Aswal, S. Lenfant, D. Guerin, J. V. Yakhmi and D. Vuillaume, *Small*, 2005, **1**, 725–729.

- 43 C.-Y. Chang, K.-T. Lee, W.-K. Huang, H.-Y. Siao and Y.-C. Chang, *Chem. Mater.*, 2015, **27**, 5122–5130.
- 44 C.-Y. Chang, W.-K. Huang, J.-L. Wu, Y.-C. Chang, K.-T. Lee and C.-T. Chen, *Chem. Mater.*, 2016, **28**, 242–251.
- 45 C.-Y. Chang, W.-K. Huang, Y.-C. Chang, K.-T. Lee and C.-T. Chen, *J. Mater. Chem. A*, 2016, **4**, 640–648.
- 46 S. Ryu, J. Seo, S. S. Shin, Y. C. Kim, N. J. Jeon, J. H. Noh and S. I. Seok, *J. Mater. Chem. A*, 2015, **3**, 3271–3275.
- 47 H. Zhang, H. Azimi, Y. Hou, T. Ameri, T. Przybilla, E. Spiecker, M. Kraft, U. Scherf and C. J. Brabec, *Chem. Mater.*, 2014, **26**, 5190–5193.
- 48 J. Min, Z.-G. Zhang, Y. Hou, C. O. Ramirez Quiroz, T. Przybilla, C. Bronnbauer, F. Guo, K. Forberich, H. Azimi, T. Ameri, E. Spiecker, Y. Li and C. J. Brabec, *Chem. Mater.*, 2015, **27**, 227–234.
- 49 F. Schreiber, *Prog. Surf. Sci.*, 2000, **65**, 151–257.
- 50 W. Chen, Y. Wu, Y. Yue, J. Liu, W. Zhang, X. Yang, H. Chen, E. Bi, I. Ashraful, M. Grätzel and L. Han, *Science*, 2015, DOI: 10.1126/science.aad1015.
- 51 G. Niu, X. Guo and L. Wang, *J. Mater. Chem. A*, 2015, **3**, 8970–8980.
- 52 N. H. Tiep, Z. Ku and H. J. Fan, *Adv. Energy Mater.*, 2016, **6**, DOI: 10.1002/aenm.201501420.
- 53 M.-C. Jung, S. R. Raga, L. K. Ono and Y. Qi, *Sci. Rep.*, 2015, **5**, 9863.
- 54 D. Song, D. Wei, P. Cui, M. Li, Z. Duan, T. Wang, J. Ji, Y. Li, J. M. Mbengue, Y. Li, Y. He, M. Trevor and N.-G. Park, *J. Mater. Chem. A*, 2016, **4**, 6091–6097.